

Theory of circular dichroism in angle-resolved resonant photoemission from magnetic surfaces

Ryunosuke Sagehashi,¹ Godeung Park,^{1,*} and Peter Krüger^{1,2,†}

¹Graduate School of Science and Engineering, Chiba University, Chiba 263-8522, Japan

²Molecular Chirality Research Center, Chiba University, Chiba 263-8522, Japan



(Received 9 November 2022; revised 25 January 2023; accepted 31 January 2023; published 8 February 2023)

A theoretical method is presented for angle-resolved photoemission at the transition metal L -edge resonance. It combines atomic multiplet calculations for the second-order resonant photoemission amplitude on the core-level site and a single scattering calculation of the photoelectron final state. The theory is applied to a magnetized Ni(111) surface excited with circularly polarized x rays at the Ni $L_{2,3}$ -edge resonance with a focus on the circular dichroism (CD) signal. Good agreement with available experimental data is achieved. It is shown that the CD pattern is composed of a slowly varying magnetic signal induced by the atomic resonant process and a signal of fast angular modulations that are due to the interference of primary and scattered waves, known as the Daimon effect. The two types of CD signals are found to be nearly additive. At the Ni L_2 -edge resonance, the angular dependence of the magnetic CD is well described by a simple expression known from x-ray magnetic CD. At the L_3 edge, however, the angular dependence is more complex and shows a pronounced final state multiplet dependence. With the present theory, it becomes possible to extract element- and site-selective magnetic information of surfaces from the CD in angle-resolved resonant photoemission data.

DOI: [10.1103/PhysRevB.107.075407](https://doi.org/10.1103/PhysRevB.107.075407)

I. INTRODUCTION

Surfaces and two-dimensional materials exhibit novel quantum phenomena related to the topology [1] and the spin-orbital polarization of the electronic states which are promising for novel electronic devices [2]. Angle-resolved photoemission spectroscopy [3–5] is commonly used to probe valence bands, but it lacks chemical and atomic structure information. When the photon energy is tuned to a strong core-valence resonance, however, the photoemission signal becomes element selective, and the valence band can be decomposed into its elemental and orbital contributions [6–8]. Therefore, resonant photoemission (RPE) effectively combines photoemission with x-ray absorption spectroscopy [9], which brings chemical and orbital selectivity. Moreover, by analyzing the angular distribution of RPE in terms of photoelectron diffraction (PED) [10], the local distribution of valence states can also be assessed, as was shown, e.g., for the in-gap states of electron-doped titania surfaces [11,12].

X-ray magnetic circular dichroism (XMCD) is a well-established technique for measuring local magnetic moments at the atomic level [13,14], but it is difficult to link the XMCD results to the atomic structure [15]. When RPE spectroscopy is performed on a magnetic system with circularly polarized light tuned to a spin-orbit split core level, then the benefits of valence photoemission and XMCD can be combined. This was demonstrated in a pioneering experiment by Morscher *et al.* [16], who measured the circular dichroism (CD) in

angle-resolved RPE from a magnetic Ni(111) surface at the Ni L_2 -edge resonance. The observed angular distribution of the CD was dominated by a dipolar term along the magnetization axis. This part of the CD signal was found to have the same angular dependence as XMCD, that is, $\Delta I_{\text{MD}} \propto \mathbf{L}_{\text{ph}} \cdot \mathbf{m}$, where \mathbf{L}_{ph} is the light helicity and \mathbf{m} is the magnetization [16]. By fitting the CD data to this expression, the magnetization axis \mathbf{m} was determined. However, the XMCD expression ΔI_{MD} does not capture the fast variations observed in the RPE CD pattern, which were attributed to the CD occurring at forward scattering peaks in PED data, known as the Daimon effect [17]. Various theoretical methods for computing RPE have been proposed [18,19], including atomic multiplet and cluster models [20,21] and first-principles methods in the independent particle picture [22,23]. To the best of our knowledge, however, none of them features the full atomic multiplet couplings in the resonant process and the diffraction of the emitted photoelectron, both of which are crucial for a quantitative analysis of the angle-resolved RPE data.

Here, we present a theory of angle-resolved RPE spectroscopy at the $L_{2,3}$ -edge resonance of transition elements. The method combines an atomic multiplet calculation for the RPE process with multiple scattering theory for the propagation of the emitted electron. We apply the theory to RPE at the $L_{2,3}$ edges of a Ni(111) surface. The results agree well with the available experimental data [16]. The CD patterns are analyzed in terms of atomic and extra-atomic contributions, resonant and nonresonant effects, and final state energy dependence. We show that there are magnetic and scattering contributions to the CD and that the two contributions are largely independent. The angular distribution of the magnetic CD can qualitatively be understood from XMCD, but at the Ni L_3 resonance there are quantitative differences, and the

*Present address: Korea Electronics Technology Institute, Seongnam-si 13509, Gyeonggi-do, Korea.

†pkruger@chiba-u.jp

RPE CD depends on the photoemission binding energy. The scattering part of the CD is due to the Daimon effect, which offers the possibility to link the magnetic information to the atomic structure around the photoemitter sites.

II. THEORY

We consider valence photoemission at the L_2 (or L_3) edge resonance. The $2p$ - $3d$ excitation is followed by the participator $L_{2,3}M_{4,5}M_{4,5}$ Auger decay, which leads to the same one-hole final state as in the direct Ni $3d$ photoemission process. To describe this process on the core-hole site, we use an atomic model with a $(3d^9)$ ground state configuration, which is the dominant contribution in Ni metal [24]. Then, the RPE process is $(3d^9) \rightarrow (2p^53d^{10}) \rightarrow (3d^8 + \epsilon)$, where ϵ denotes the high-energy continuum state of the emitted electron. The emission intensity is computed by second-order time-dependent perturbation theory, using the Kramer-Heisenberg formula [21,25]. The perturbation consists of the electron-photon interaction, which is responsible for direct photoemission and core-level excitation, and the electron-electron Coulomb interaction with a continuum state, which gives rise to the autoionization decay. The emission intensity is

$$I \propto \sum_{fg} |T_{fg}(\omega)|^2 \delta(E_f - E_g - \hbar\omega), \quad (1)$$

where the sums run over all degenerate ground and final states and the resonant amplitude T_{fg} is given, in second-order perturbation, by [21–23,26]

$$T_{fg}(\omega) = \langle f|D|g\rangle + \sum_m \frac{\langle f|V_A|m\rangle\langle m|D|g\rangle}{\hbar\omega + E_g - E_m - i\Gamma_m}. \quad (2)$$

Here, $\hbar\omega$ is the photon energy, and $|g\rangle$, $|m\rangle$, and $|f\rangle$ are ground, intermediate, and final states with energies E_g , E_m , and E_f , respectively. The m sum runs over all $2p$ - $3d$ excited states, and Γ_m are their lifetime widths. Here, we take Γ as a state-independent parameter and set it to 1 eV in all calculations. D denotes electron-photon interaction, which we describe in electric dipole approximation and length form, i.e., $D = \mathbf{e} \cdot \mathbf{r}$, where \mathbf{e} is the light polarization vector. V_A denotes the Coulomb interaction responsible for autoionization decay.

The calculation is carried out in two steps. First, the resonant transition matrix elements are computed for a single Ni atom using multiplet theory [27,28], and second, the various waves of the emitted electron are taken as source waves in a finite-cluster multiple scattering calculation. In the atomic calculation, we consider the electronic configurations $(2p^63d^9)$ for ground states, $(2p^53d^{10})$ for intermediate states, and $(2p^63d^8\epsilon l^1)$ for final states. Here, ϵl denotes a high-energy (ϵ) continuum orbital of angular momentum l , describing the photoelectron wave. By energy conservation we have $\epsilon = \hbar\omega + E_g - E_f^{N-1}$, where E_f^{N-1} is the energy of one of the $(2p^63d^8)$ multiplet states. For the multiplet calculation, we use the parameter values given by Tanaka and Jo [21] which were obtained with single-atom Hartree-Fock calculations. However, the $3d$ spin-orbit coupling is set to zero in order to obtain a realistic ground state of metallic Ni with

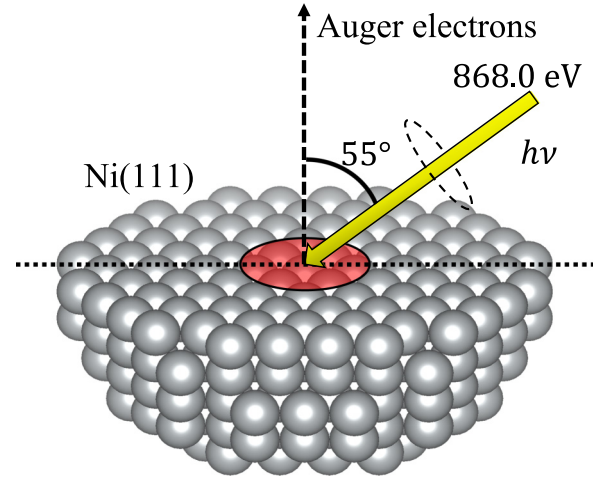


FIG. 1. Cluster model used in the calculation for the Ni(111) surface. Atoms located near the central axis below the red circle are taken as electron emitters. As in the experiment in Ref. [16], light incidence and electron emission directions are fixed at a relative angle of 55° while the sample is rotated.

a small orbital moment. This atomic ground state is fivefold degenerate, with the down-spin hole occupying any one of the $3d$ orbitals. Final states are taken as the product of a $(3d^8)$ multiplet state and a photoelectron wave.

In the atomic calculation, we first consider a basis final state $|f(lms)\rangle$ which is the product state between an $N-1$ electron eigenstate of the photoionized atom [i.e., one of the 45 $(3d^8)$ eigenstates in the present case] and a photoelectron orbital $\phi_{lms}(\mathbf{r})$, i.e., a spherical wave with angular momenta lm , spin s , and energy $\epsilon = \hbar\omega + E_g - E_f^{N-1}$. For the $L_{2,3}M_{4,5}M_{4,5}$ Auger decay, possible emitted electron angular momenta are $l = 1, 3, 5$. The resonant amplitudes for these states are computed using Eq. (2) and are denoted by $T_{f(lms),g}$. The resonantly emitted photoelectron waves from a single atom are then given by

$$\phi_{fg}(\mathbf{r}) = \sum_{lms} T_{f(lms),g} \phi_{lms}(\mathbf{r}). \quad (3)$$

The waves $\phi_{fg}(\mathbf{r})$ are taken, one at a time, as the source wave in a PED calculation carried out with the multiple scattering code EDAC [29]. Here, we used the single scattering approximation, which leads to good results for x-ray PED at kinetic energies above 500 eV [30]. For lower energies, multiple scattering effects can be important, especially for polarization-dependent angle-resolved photoemission spectroscopy (including CD) [31,32]. As a test, we computed the CD patterns of selected final states with multiple scattering theory up to fifth order (not shown) and found only small differences compared to the single scattering result.

Figure 1 shows the cluster model used for the PED calculation. It is a hemispherical cluster with a radius of 10 Å containing 321 Ni atoms. For each atomic layer, emitter atoms were chosen near the central axis, and the contributions of each layer were summed. Damping of the photoelectron wave was taken into account with an inelastic mean free path of 1 nm. In the scattering calculation, the atomic potentials (except for the emitter atom) were not considered to be spin

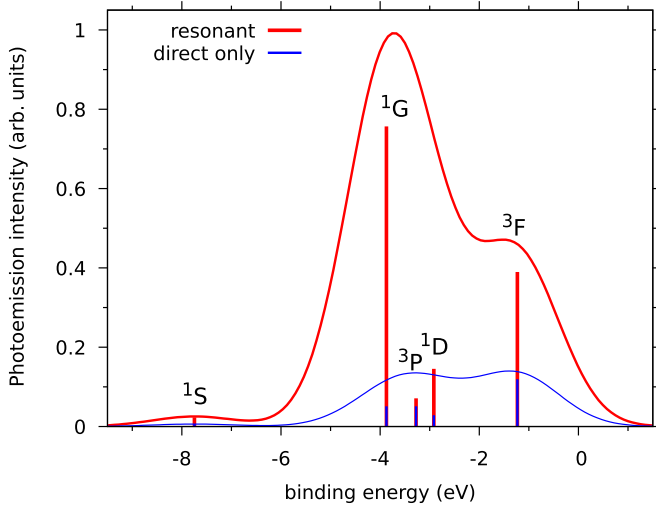


FIG. 2. RPE spectrum at the Ni L_2 -edge resonance for a Ni atom with the ($3d^9$) ground state calculated with atomic multiplet theory. The total RPE intensity (thick red lines) and the contribution of the direct photoemission process (thin blue lines) are shown as line spectra and Gaussian broadened spectra with a FWHM of 2 eV.

polarized for simplicity. We have checked that the spin polarization of the scattering Ni atoms has a negligible effect on the results. In the calculation, the experimental geometry and the way the sample is rotated are exactly the same as in the experiment by Morscher *et al.* [16]. Also, as in the experiment, a magnetic field of 2 T was applied along the $[\bar{1}10]$ direction of the Ni(111) surface, leading to full spin polarization of the ($3d^9$) ground state of the emitter atom along the magnetization axis.

III. RESULTS AND DISCUSSION

Figure 2 shows the energy distribution curve of the RPE intensity at the Ni L_2 -edge resonance (photon energy of 868 eV) as obtained with the atomic multiplet calculation. The contribution of the direct photoemission process [first term on the right-hand side of Eq. (2)] is also shown. The spectrum corresponds to a spherical average over emission angles and light polarizations. From the line spectrum in Fig. 2 one can clearly see the five multiplet levels of the ($3d^8$) final state configuration. The energy splittings and relative intensities of the five multiplets ($1S$, $1G$, $3P$, $1D$, $3F$) in Fig. 2 are typical for the LMM Auger decay of nickel [33]. To account for the final state lifetime and band width in Ni metal, the line spectrum has been broadened with a Gaussian with a FWHM of 2 eV (red line). The broadened spectrum agrees well with the available experimental data [33], demonstrating the validity of the present multiplet model.

Figure 3 shows PED patterns at the Ni L_2 -edge resonance, computed with the cluster model, along with experimental data taken from Ref. [16]. Here, a “pattern” is a stereographic projection of the intensity distribution as a function of emission angle. In Fig. 3, the intensities of all ($3d^8$) final states are summed, corresponding to the photoemission intensity integrated over the whole valence band (or the whole L_2MM peak). The maximum polar angle is $\theta = 70^\circ$.

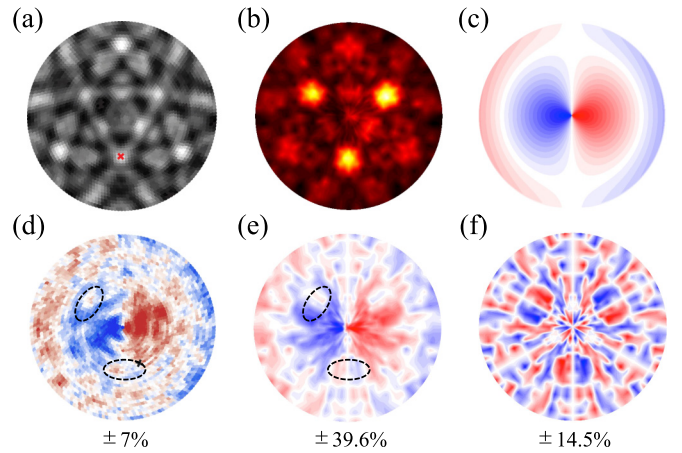


FIG. 3. Diffraction patterns and corresponding circular dichroism (CD) for RPE from Ni(111) at the Ni L_2 edge. The patterns are stereographic projections in the polar angle range $\theta < 70^\circ$. The magnetization axis is taken as $[\bar{1}10]$ and corresponds to the horizontal (x) axis of the plots. (a) Experimental diffraction pattern obtained with circularly polarized light (positive helicity). (b) Corresponding calculated pattern. (c) Angular plot of the function $\mathbf{L} \cdot \mathbf{m}$, i.e., the empirical model for CD used in [16]. (d) Experimental CD pattern (asymmetry function). Two of the three first-nearest-neighbor focusing peaks are surrounded by dashed ellipses. The observed CD sign change at these peaks is typical for the Daimon effect. (e) Corresponding calculated CD pattern. (f) Theoretical CD pattern for a nonmagnetic ground state. In (d)–(f) the maximum anisotropy (corresponding to red and blue colors) is indicated below the plot. The experimental patterns in (a) and (d) are taken from Ref. [16] and have been rotated to match our reference frame.

The experimental resonant PED pattern [16] obtained with circular polarization (positive helicity) is shown in Fig. 3(a), and the corresponding calculation is given in Fig. 3(b). The peak positions agree very well, while the agreement of the peak intensities is fair. The three brightest spots in Fig. 3(b) are forward focusing peaks corresponding to the fcc nearest-neighbor directions along $[110]$ and equivalent axes. The PED patterns in Figs. 3(a) and 3(b) show approximately threefold symmetry. The fcc(111) surface has C_{3v} symmetry, but due to in-plane magnetization and to circular polarization and the oblique incidence of the light, the patterns do not have exact C_{3v} symmetry.

Following Ref. [16] we represent the CD by using the asymmetry function

$$A = \frac{I_+ - I_-}{I_+ + I_-}. \quad (4)$$

Here, I_σ is the photoemission intensity for circularly polarized light with helicity $\sigma\hbar$, $\sigma = \pm 1$. In Eq. (4) the CD is normalized by the total emission intensity such that the fast intensity variation due to the PED effect is removed.

The experimental and calculated CD patterns are shown in Figs. 3(d) and 3(e), respectively. The overall sign (red-blue) distribution agrees very well, and much of the fast intensity modulation is also similar between theory and experiment. In particular, the CD signal varies very fast as a function of azimuthal angle around forward scattering peaks. This is most

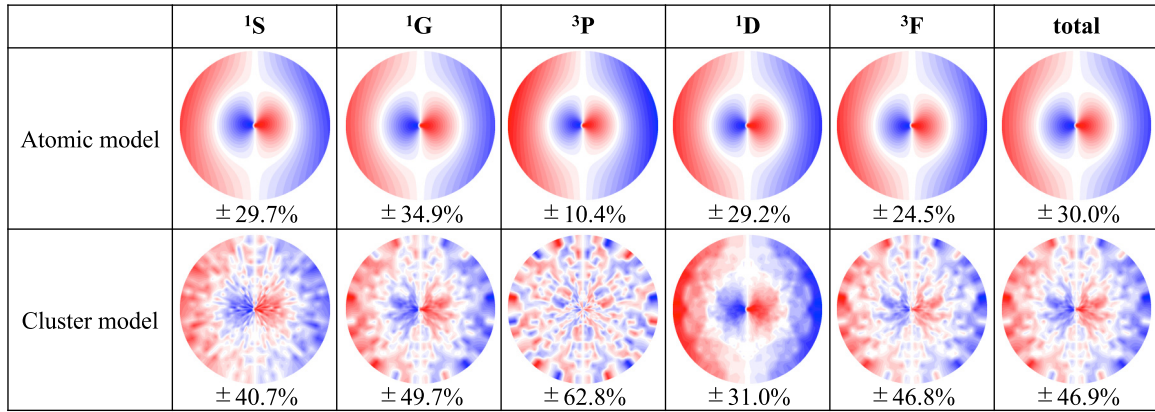


FIG. 4. Theoretical CD patterns of L_2 -edge RPE from Ni(111) in RPE for each (d^8) final state term. Top row: atomic model; bottom row: cluster model. The binding energy of the five multiplet terms decreases from left to right; see Fig. 2 for the exact energy positions. The pattern “total” corresponds to the energy integrated photoemission intensity. The maximum anisotropy values [Eq. (4)] are indicated in percent under each pattern. The full hemisphere, $\theta < 90^\circ$, is shown.

clearly seen at the first-nearest-neighbor focusing peaks, two of which are highlighted by dashed ellipses in Figs. 3(d) and 3(e). This feature is well reproduced in the calculation. The CD sign change is indicative of the Daimon effect, which is well known for core-level PED [17]. The maximum CD anisotropy is much larger in theory (40%) than in experiment (7%), and the calculation does not reproduce all the fine structure of the experimental pattern. This is partly because in the experiment [16], the sample was magnetized only to about 40%. Other sources of disagreement may include noise in the data and various approximations used in the theory. The CD patterns in Figs. 3(c) and 3(d) are dominated by a slowly varying distribution which has an approximately cylindrical symmetry around the in-plane magnetization axis $[110]$ (horizontal in the stereographic plot). In Ref. [16], the magnetic CD was modeled by the function $\Delta I_{MD} \propto \mathbf{L}_{ph} \cdot \mathbf{m}$, which is the angular dependence of x-ray magnetic CD in absorption. Here, \mathbf{L}_{ph} is the light helicity vector, and \mathbf{m} is the sample magnetization. The function ΔI_{MD} is plotted in Fig. 3(c). It is seen that this simple expression captures well the slowly varying part of the CD patterns in Figs. 3(d) and 3(e).

In order to understand the effect of magnetism on the CD pattern, we repeated the cluster calculation with zero magnetic field, i.e., with a Ni emitter in a nonmagnetic ground state. The result is shown in Fig. 3(f). Clearly, the slowly varying contribution to the CD is absent, proving that this part of the CD is indeed of magnetic origin. It follows that CD in resonant PED can be used to probe magnetism, as proposed in Ref. [16]. The CD pattern of the nonmagnetic surface [Fig. 3(f)] displays a C_3 symmetry, which reflects the C_{3v} symmetry of the fcc(111) surface, while the mirror plane is absent because of the circular polarization of the light. The patterns of the magnetic surface [Figs. 3(b) and 3(e)] have no (exact) symmetry because the magnetization axis in the surface plane breaks the threefold symmetry. The CD map of the nonmagnetic surface [Fig. 3(f)] has a complex structure in which the largest dichroism is seen around forward focused peaks where the CD changes sign when the peak is crossed in an azimuthal scan. This is a clear indication of the Daimon effect, which was

recently observed in resonant Auger diffraction from Ni and Cu surfaces [33–35].

The CD patterns in Figs. 3(e) and 3(f) were calculated with the full cluster model, including the atomic resonant process and the diffraction of the emitted photoelectron. In order to better understand the origin of the dichroism, we also computed CD patterns from the atomic multiplet model alone, neglecting photoelectron scattering. Moreover, we analyzed the energy dependence of the CD by calculating the CD patterns for the five different binding energies corresponding to the multiplet terms of the ($3d^8$) final state.

The results are shown in Fig. 4 for both the atomic multiplet model (top row) and the cluster calculation (bottom row). In the atomic calculation, the maximum CD (anisotropy value) varies considerably between five (d^8) multiplets. The angular distribution, however, is almost independent of the final state. Then it must be determined by the initial and intermediate states, i.e., the states involved in the x-ray absorption process. This may explain why the angular dependence of XMCD [$\mathbf{L}_{ph} \cdot \mathbf{m}$; Fig. 3(c)] also fits well the magnetic CD in RPE [Figs. 3(d) and 3(e)]. Turning now to the cluster calculations (bottom row in Fig. 4), it is seen that the patterns differ considerably between different multiplet terms in terms of both maximum asymmetry and angular distribution. Comparing the atomic and cluster patterns immediately shows that the fine structure in the cluster pattern is due to photoelectron scattering, as anticipated by the Daimon effect. Since the atomic photoelectron wave $\phi(\mathbf{r})$ in Eq. (3) has a different angular momentum decomposition for each (d^8) multiplet, it is not surprising that the CD pattern changes from one term to the other.

In order to assess the relative role played in the CD formation by the direct photoemission process and the resonant process, we calculated them separately by setting either the direct amplitude [first term on the right-hand side of Eq. (2)] or the resonant amplitude (second term) to zero. The CD patterns in Fig. 5 correspond to a single-atom calculation with only the resonant process (top row) and a cluster calculation with only the resonant process (middle row) or with only the direct process (bottom row). The single-atom calculation with only the

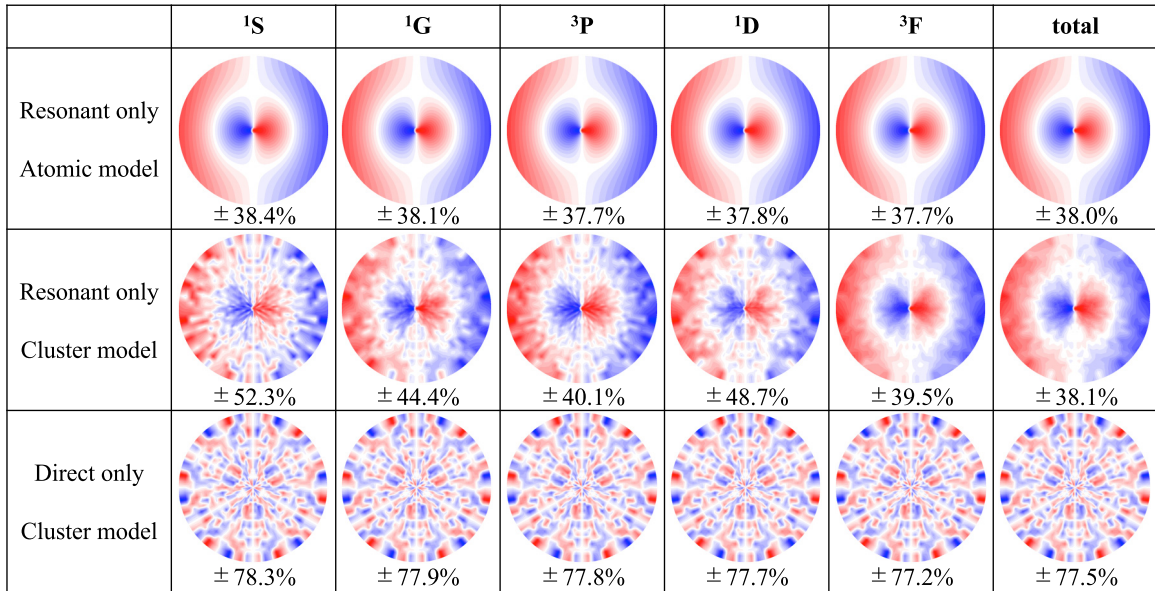


FIG. 5. CD patterns of L_2 -edge RPE decomposed into resonant and direct process, i.e., computed with only the first or only the second term on the right-hand side of Eq. (2). Top row: resonant process in only the atomic model. Middle row: resonant process in only the cluster model. Bottom row: direct process in only the cluster model.

direct process is not shown because the CD is exactly zero in the present model, where the weak Ni $3d$ spin-orbit coupling has been neglected. There is only a little change among the rows in Fig. 5, which means that both for the L_2 -edge resonant process alone and for the direct process alone, the final state dependence of the CD pattern is very weak. Therefore, the substantial final state dependence of the CD pattern which is observed in the full calculation (Fig. 4, bottom row) is due to the interplay between the resonant and direct channels. As seen in Fig. 2, the intensity ratio between direct and resonant channel changes a great deal between the different final state multiplets. When the resonant enhancement is strong (e.g., for the 1G state) the resonant channel dominates the full CD pattern, but when the resonant effect is very weak such as for the 1P state, the direct process dominates. The results in Figs. 4 and 5 thus clearly show that both the direct and resonant emission processes contribute to the Daimon effect but their relative importance strongly depends on the final state multiplet. This is in line with the observation by Matsui *et al.* [33] that in Ni $L_3M_{4,5}M_{4,5}$ and Ni $L_3M_{2,3}M_{4,5}$ resonant Auger emission from nonmagnetized nickel, the intensity of the Daimon effect strongly depends on the binding energy.

It is interesting to note that the atomic CD patterns (top row of Fig. 4) are virtually independent of the final state and agree almost perfectly with the XMCD expression $\mathbf{L}_{\text{ph}} \cdot \mathbf{m}$ plotted in Fig. 3(c). We note that this is a special feature of the Ni L_2 -edge resonance. It does not hold in general, as will be shown below in the case of the Ni L_3 edge.

In order to examine the effect of electron scattering, we compute the CD from the RPE intensity difference between the cluster and the single atom. The patterns are shown in the top row of Fig. 6 for the five final state multiplets and for the total L_2 -edge peak. It is seen that the smoothly varying part of the CD is gone and only the fast angular modulations, which can be attributed to the Daimon effect, remain. For comparison the bottom row of Fig. 6 shows the theoretical

CD patterns of the nonmagnetic surface (without any subtraction). The patterns in the top and bottom rows of Fig. 6 are very similar, indeed almost identical, except for 1D , whose nonmagnetic CD is extremely weak. This shows that there are two very different origins for CD in resonant PED. First, there is magnetic CD, which is a direct consequence of XMCD since resonant Auger emission includes x-ray absorption as the excitation process. Second, there is CD due to Auger and photoelectron scattering, i.e., the Daimon effect [17,35]. The analysis in Figs. 4 and 5 shows that these two phenomena are largely independent in the case of Ni L_2 -edge resonant PED. This is rather intuitive since XMCD involves only the initial and intermediate states and is essentially an intra-atomic effect, while the Daimon effect is genuinely extra-atomic and involves only the final state.

We now turn to the Ni L_3 -edge resonance (photon energy 850 eV). The CD patterns of the atomic and cluster calculation are shown in Fig. 7. The atomic pattern from the integrated photoemission peak (top row, total column) has the opposite sign with respect to the L_2 resonance in Fig. 5. This is expected from the fact that the XMCD signal generally changes sign when going from the L_2 to the L_3 edge as a consequence of the opposite spin-orbit couplings of the $2p_{1/2}$ and $2p_{3/2}$ states. Further, in contrast to the L_2 edge, the atomic CD patterns of the L_3 -edge resonance change considerably between the different final state multiplets. While the topology of the patterns is the same, the position of the circular nodal lines (zero CD, white) varies enormously from $\theta \sim 90^\circ$ for 1S to $\theta \sim 10^\circ$ for 3F . Similar differences are also seen in the CD patterns of the cluster calculation (Fig. 7, bottom row). In light of these results, the absence of any final state dependence of the atomic CD in the at the Ni L_2 -edge resonance must be seen as a special case rather than a general rule.

Finally, we discuss the validity of the empirical model $\Delta I_{MD} \sim \mathbf{L}_{\text{ph}} \cdot \mathbf{m}$ introduced in Ref. [16]. We note that this expression correctly describes the angular dependence of

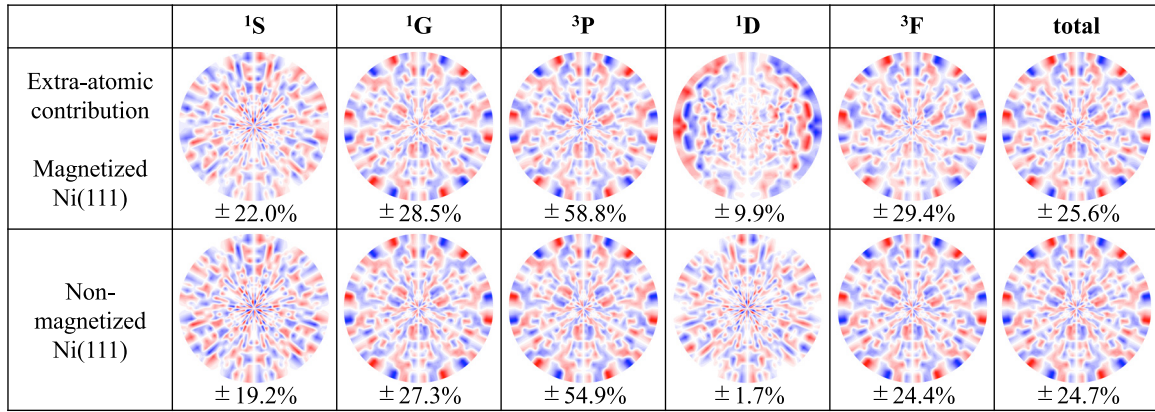


FIG. 6. CD patterns of L_2 -edge RPE: scattering contribution vs nonmagnetic signal. Top row: extra-atomic contribution to CD patterns of the magnetized Ni(111) surface. Before calculating the anisotropy, the single-atom emission intensity was subtracted from the cluster intensity. Bottom row: CD patterns of the nonmagnetized Ni(111) surface (cluster calculation without any subtraction).

XMCD, but for resonant Auger emission, it is an approximation, even for the free atom. The experiments in Ref. [16] and the present calculations indicate that the empirical model is a very good approximation for the magnetic contribution to the CD at the Ni L_2 resonance. At the L_3 edge, however, the model is much less reliable. While it roughly fits the peak integrated atomic CD (Fig. 7, total column), it fails to account for the strong final state dependence of the CD pattern.

Nonetheless, all atomic CD patterns at the L_2 and L_3 resonances (Figs. 6 and 7) have the same topology as the empirical model, with two nodal lines, one vertical straight line, and one circle. The occurrence of these shapes can be understood from symmetry alone. In the model, the nodal lines are determined by the condition $\mathbf{L}_{\text{ph}} \cdot \mathbf{m} = 0$. As \mathbf{m} defines the x axis, \mathbf{L}_{ph} must lie in the xz plane. In the experimental geometry of Ref. [16], where \mathbf{L}_{ph} and the electron emission vector \mathbf{k} make a fixed angle of 55° (Fig. 1), this implies a relation $[f(\theta, \phi) = 0]$ between angles θ and ϕ of \mathbf{k} . The angles that satisfy this relation appear as two lines on the stereographic projection, namely, a vertical line through the center and a circle at $\theta = 55^\circ$ [16]. For the vertical line, the emission direction \mathbf{k} is perpendicular to the magnetization axis \mathbf{m} , i.e.,

$\mathbf{k} \cdot \mathbf{m} = 0$, but this does not hold for the circle, where \mathbf{k} and \mathbf{m} have no special relation.

In the following, we consider a single Ni atom since we have seen that this is sufficient to describe the magnetic CD. What is the effect of helicity reversal $\mathbf{L}_{\text{ph}} \rightarrow -\mathbf{L}_{\text{ph}}$ for the points with $\mathbf{L}_{\text{ph}} \cdot \mathbf{m} = 0$? To understand this, we apply a mirror operation $x \rightarrow -x$ to the system. This operation leaves the atomic ground state invariant since the magnetization \mathbf{m} is an axial vector. Therefore, the photoemission intensity of the mirrored system is the same as that of the original system. Under the mirror operation the helicity (axial vector \mathbf{L}_{ph} in the mirror plane) is reversed, while the emission vector \mathbf{k} becomes $\mathbf{k}' = (-k_x, k_y, k_z)$. This means that in the case with $\mathbf{m} \sim x$, $\mathbf{L}_{\text{ph}} \cdot \mathbf{m} = 0$, we have $I_+(k_x, k_y, k_z) = I_-(-k_x, k_y, k_z)$, where I_{\pm} is the photoemission intensity for positive and negative helicity. The immediate consequence is that $I_+ = I_-$ for $k_x = 0$, which proves that the CD must vanish along the vertical line ($k_x = 0$), as was observed experimentally and theoretically in all cases. For the other points where $\mathbf{L}_{\text{ph}} \cdot \mathbf{m} = 0$ (circle) we have $k_x \neq 0$, and so we cannot conclude from the above symmetry argument that the CD must vanish. The calculations show that the CD does vanish on a circle around the center, but the radius of this circle depends on the core edge (L_2 or L_3)

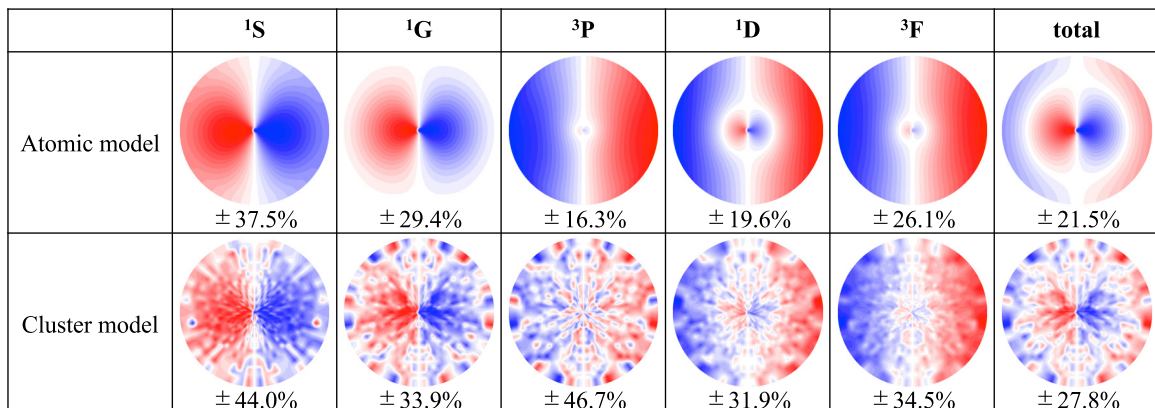


FIG. 7. Calculated CD patterns of RPE at the L_3 edge. Top row: atomic model. Bottom row: cluster model.

and on the final state multiplet. It is not simply determined by the condition $\mathbf{L}_{\text{ph}} \cdot \mathbf{m} = 0$.

In conclusion of this section, the XMCD angular dependence $I_{MD} \sim \mathbf{L}_{\text{ph}} \cdot \mathbf{m}$ determines the topology of the atomic CD in Ni L -edge RPE, and it correctly predicts that the CD vanishes along the vertical line, where both \mathbf{k} and \mathbf{L}_{ph} are perpendicular to the magnetization axis. It also describes surprisingly well the angular dependence of the atomic CD in RPE at the Ni L_2 edge but fails to do so at the L_3 edge. This means that in general, the magnetic CD in RPE cannot be reduced to that of XMCD and the final state dependence cannot be neglected, even for a free atom. The magnetic CD needs to be calculated by explicitly taking into account the Auger decay process, which can conveniently be done using the present theory.

IV. CONCLUSIONS

In summary, we have presented a theory for angle-resolved RPE and its CD by combining atomic multiplet theory and single scattering calculations. The method was applied to the Ni $L_{2,3}$ -edge resonances at the Ni(111) surface, and good agreement with available experimental data was obtained. The CD patterns contain a slowly varying signal of magnetic origin and fast angular modulations due to the interference of primary and scattered waves. Our results indicate that these

two parts of the CD signal are essentially independent, which makes it easy to separate the magnetic information from the structural information contained in the data. The CD pattern due to the photoelectron scattering (Daimon effect) has a complex dependence on the final state energy, suggesting that the angular momentum transfer from the photon to the photoelectron is strongly influenced by multiplet effects. At the Ni L_2 edge, the angular dependence of the magnetic CD is independent of the final state and well accounted for by a simple expression valid for XMCD. At the L_3 edge, however, the magnetic CD pattern strongly depends on the final state energy, and the angular dependence cannot be reduced to that of XMCD. The present work provides a framework for the quantitative analysis of angle-resolved resonant photoemission and its circular dichroism. Since this spectroscopic technique combines chemical, structural, and magnetic information in a unique way, its theoretical understanding will create interesting possibilities for atomically resolved characterization of magnetic species at surfaces and interfaces.

ACKNOWLEDGMENTS

We thank Dr. J. García de Abajo for making his EDAC software available to us. R.S. acknowledges support by the Japan Science and Technology Agency (JST) with the establishment of university fellowships towards the creation of science technology innovation, Grant No. JPMJFS2107.

-
- [1] J. Moore, *Nature (London)* **464**, 194 (2010).
 [2] E. C. Ahn, *npj 2D Mater Appl* **4**, 17 (2020).
 [3] A. Damascelli, Z. Hussain, and Z.-X. Shen, *Rev. Mod. Phys.* **75**, 473 (2003).
 [4] K. Sakamoto, H. Ishikawa, T. Wake, C. Ishimoto, J. Fujii, H. Bentmann, M. Ohtaka, K. Kuroda, N. Inoue, T. Hattori, T. Miyamachi, F. Komori, I. Yamamoto, C. Fan, P. Krüger, H. Ota, F. Matsui, F. Reinert, J. Avila, and M. C. Asensio, *Nano Lett.* **21**, 4415 (2021).
 [5] R. Ono, A. Marmodoro, J. Schusser, Y. Nakata, E. F. Schwier, J. Braun, H. Ebert, J. Minár, K. Sakamoto, and P. Krüger, *Phys. Rev. B* **103**, 125139 (2021).
 [6] N. Mårtensson, M. Weinelt, O. Karis, M. Magnuson, N. Wassdahl, A. Nilsson, J. Stöhr, and M. Samant, *Appl. Phys. A* **65**, 159 (1997).
 [7] T. R. F. Peixoto, H. Bentmann, S. Schreyeck, M. Winnerlein, C. Seibel, H. Maaß, M. Al-Baidhani, K. Treiber, S. Schatz, S. Grauer, C. Gould, K. Brunner, A. Ernst, L. W. Molenkamp, and F. Reinert, *Phys. Rev. B* **94**, 195140 (2016).
 [8] F. Alarab, K. Hricovini, B. Leikert, L. Nicolai, M. Fanciulli, O. Heckmann, C. Richter, L. Prušakova, Z. Jansa, P. Šutta, J. Rault, P. Lefevre, M. Sing, M. Muntwiler, R. Claessen, and J. Minár, *Phys. Rev. B* **104**, 165129 (2021).
 [9] M. Weinelt, A. Nilsson, M. Magnuson, T. Wiell, N. Wassdahl, O. Karis, A. Föhlisch, N. Mårtensson, J. Stöhr, and M. Samant, *Phys. Rev. Lett.* **78**, 967 (1997).
 [10] A. Verdini, P. Krüger, and L. Floreano, *Resonant Photoelectron Diffraction* (Springer, Berlin, 2013), Chap. 8, pp. 217–247.
 [11] P. Krüger, S. Bourgeois, B. Domenichini, H. Magnan, D. Chandresris, P. Le Fèvre, A. M. Flank, J. Jupille, L. Floreano, A. Cossaro, A. Verdini, and A. Morgante, *Phys. Rev. Lett.* **100**, 055501 (2008).
 [12] P. Krüger, J. Jupille, S. Bourgeois, B. Domenichini, A. Verdini, L. Floreano, and A. Morgante, *Phys. Rev. Lett.* **108**, 126803 (2012).
 [13] B. T. Thole, P. Carra, F. Sette, and G. van der Laan, *Phys. Rev. Lett.* **68**, 1943 (1992).
 [14] P. Carra, B. T. Thole, M. Altarelli, and X. Wang, *Phys. Rev. Lett.* **70**, 694 (1993).
 [15] K. Amemiya, S. Kitagawa, D. Matsumura, H. Abe, T. Ohta, and T. Yokoyama, *Appl. Phys. Lett.* **84**, 936 (2004).
 [16] M. Morscher, F. Nolting, T. Brugger, and T. Greber, *Phys. Rev. B* **84**, 140406 (2011).
 [17] H. Daimon, *Phys. Rev. Lett.* **86**, 2034 (2001).
 [18] C. Janowitz, R. Manzyk, M. Skibowski, Y. Takeda, Y. Miyamoto, and K. Cho, *Surf. Sci.* **275**, L669 (1992).
 [19] Y. Kucherenko, B. Sinković, E. Shekel, P. Rennert, and S. Hulbert, *Phys. Rev. B* **62**, 5733 (2000).
 [20] G. van der Laan, M. Surman, M. A. Hoyland, C. F. J. Flipse, B. T. Thole, Y. Seino, H. Ogasawara, and A. Kotani, *Phys. Rev. B* **46**, 9336 (1992).
 [21] A. Tanaka and T. Jo, *J. Phys. Soc. Jpn.* **63**, 2788 (1994).
 [22] F. Da Pieve and P. Krüger, *Phys. Rev. Lett.* **110**, 127401 (2013).
 [23] F. Da Pieve and P. Krüger, *Phys. Rev. B* **88**, 115121 (2013).
 [24] T. Jo and G. A. Sawatzky, *Phys. Rev. B* **43**, 8771 (1991).
 [25] L. C. Davis and L. A. Feldkamp, *Phys. Rev. B* **23**, 6239 (1981).

- [26] A. W. Kay, F. J. Garcia de Abajo, S.-H. Yang, E. Arenholz, B. S. Mun, N. Mannella, Z. Hussain, M. A. Van Hove, and C. S. Fadley, *Phys. Rev. B* **63**, 115119 (2001).
- [27] F. de Groot and A. Kotani, *Core Level Spectroscopy of Solids* (CRC Press, Boca Raton, FL, 2008).
- [28] A. K. Shukla, P. Krüger, R. S. Dhaka, D. I. Sayago, K. Horn, and S. R. Barman, *Phys. Rev. B* **75**, 235419 (2007).
- [29] F. J. García de Abajo, M. A. Van Hove, and C. S. Fadley, *Phys. Rev. B* **63**, 075404 (2001).
- [30] C. S. Fadley, *Prog. Surf. Sci.* **16**, 275 (1984).
- [31] M. R. Scholz, J. Sánchez-Barriga, J. Braun, D. Marchenko, A. Varykhalov, M. Lindroos, Y. J. Wang, H. Lin, A. Bansil, J. Minár, H. Ebert, A. Volykhov, L. V. Yashina, and O. Rader, *Phys. Rev. Lett.* **110**, 216801 (2013).
- [32] P. Krüger and F. Matsui, *J. Electron Spectrosc. Relat. Phenom.* **258**, 147219 (2022).
- [33] F. Matsui, H. Ota, and K. Sugita, *Phys. Rev. B* **97**, 035424 (2018).
- [34] F. Matsui, M. Fujita, T. Ohta, N. Maejima, H. Matsui, H. Nishikawa, T. Matsushita, and H. Daimon, *Phys. Rev. Lett.* **114**, 015501 (2015).
- [35] F. Matsui, N. Maejima, H. Matsui, H. Nishikawa, H. Daimon, T. Matsushita, M. Muntwiler, R. Stania, and T. Greber, *Z. Phys. Chem.* **230**, 519 (2016).